Electronic Supplementary Information

Novel Concept of Two-Component Dielectric Function for Gold Nanostars: Theoretical Modelling and Experimental Verification

Nikolai G. Khlebtsov,[1,2,*] *Sergey V. Zarkov,*[3] *Vitaly A. Khanadeev,*[1] *Yuri A. Avetisyan*[3]

[1]*Institute of Biochemistry and Physiology of Plants and Microorganisms, Russian Academy of Sciences, 13 Prospekt Entuziastov, Saratov 410049, Russia*

[2]*Saratov State University, 83 Ulitsa Astrakhanskaya, Saratov 410012, Russia*

[3]*Institute of Precision Mechanics and Control, Russian Academy of Sciences, Saratov 410028, 24 Ulitsa Rabochaya, Russia*

*Corresponding author: khlebtsov@ibppm.ru

Content.

Section S1. Size-corrected dielectric function of gold nanoparticles

For spikes, Eq. (2) of the main text can be rewritten as

$$\Delta\varepsilon(\omega,\mathbf{r},l_s)\equiv\Delta\varepsilon(\omega,l_s)=\frac{\omega_p^2}{\omega(\omega+i\gamma_b)}-\frac{\omega_p^2}{\omega(\omega+i\gamma_s)}, \tag{S1}$$

where $\gamma_s=\gamma_b+A_s v_F/l_s$ is the damping parameter, the damping constant A_s includes the surface electron scattering and the chemical interface dumping contributions. The separation of Eq. (S1) into real and imaginary parts gives

$$\Delta\varepsilon(\omega,l_s)=\frac{\omega_p^2}{\omega^2}\left[\frac{1}{(1+\gamma_b^2/\omega^2)}-\frac{1}{(1+\gamma_s^2/\omega^2)}\right]+i\frac{\omega_p^2}{\omega^2}\left[\frac{\gamma_s/\omega}{(1+\gamma_s^2/\omega^2)}-\frac{\gamma_b/\omega}{(1+\gamma_b^2/\omega^2)}\right]. \tag{S2}$$

Under conditions $\gamma_s^2/\omega^2<<1$, $\gamma_b^2/\omega^2<<1$, we arrive at:

$$\Delta\varepsilon(\omega,l_s)=\left|\Delta\varepsilon''\right|\left(\frac{\gamma_s+\gamma_b}{\omega}+i\right), \tag{S3}$$

$$\left|\Delta\varepsilon''\right|=\frac{\omega_p^2}{\omega^3}\left[\gamma_s-\gamma_b\right]=\frac{\omega_p^2}{\omega^3}A_s\frac{v_F}{l_s}=\frac{\lambda^3}{2\pi c\lambda_p^2}A_s\frac{v_F}{l_s}, \tag{S4}$$

where $\lambda_p=2\pi c/\omega_p$ is plasma wavelength, c is the speed of light.

The first term in Eq. (S3) can be rewritten as

$$B=\frac{\gamma_a+\gamma_b}{\omega}=\frac{(2\gamma_b+Av_F/l_s)\lambda}{2\pi c}=\left(1.06\overline{\gamma}_b+7.48A_s/l_s\right)10^{-4}\lambda, \tag{S5}$$

where l_s and λ are expressed in nm, and the normalized parameter $\overline{\gamma}_b$ is defined by relationship

$$\overline{\gamma}_b=\gamma_b\times10^{-14}(\text{s/nm}). \tag{S6}$$

Because the dimension of γ_b is s^{-1}, the dimension of $\overline{\gamma}_b$ is nm^{-1}. Similarly, Eq. (S4) can be normalized as follows

$$\left|\Delta\varepsilon''\right|=\frac{\lambda^3}{2\pi c\lambda_p^2}A_s\frac{v_F}{l_s}=5.37(\text{nm})\frac{A_s}{l_s(\text{nm})}\left(\frac{\lambda}{520}\right)^3, \tag{S7}$$

where the wavelength is expressed in nm and normalized to the LPR wavelength of small gold spheres in water. Finally, combining (S3), (S5) and (S7) we get

$$\Delta\varepsilon(\omega, l_s) = \left|\Delta\varepsilon''\right|\left(B + i\right), \tag{S8}$$

where $\left|\Delta\varepsilon''\right|$ and B are defined by normalized Eqs. (S5) and (S7).

Table 1 summarizes the literature data for bulk parameters of gold. The average value of plasma frequency is $\hbar\omega_p = 9.0 \pm 0.38$ eV. In Table 1, the damping constant $\gamma_b = 1.64 \times 10^{14}\,\mathrm{s}^{-1}$ seems to be overestimated compared with other literature data. The average value of the damping constant equals $\gamma_b = (1.02 \pm 0.17) \times 10^{14}\,\mathrm{s}^{-1}$, where the first value has not been taken into account.

Table S1. Parameters of the Lorenz-Drude model for bulk gold

$\hbar\gamma_b$ eV	γ_b $10^{14}\,\mathrm{s}^{-1}$	$\hbar\omega_p$ eV	ω_p $10^{16}\,\mathrm{s}^{-1}$	λ_p nm	Refs.
0.108	1.64	8.85	1.34	140	[1]
0.0708	1.08	9.48	1.37	138	[2]
0.0708	1.08	9.48	1.44	131	[3]
0.0691	1.05	8.95	1.36	139	[4]
0.0829	1.26	8.71	1.32	143	[5]
0.047* 0.055**	0.714* 0.833**	8.45	1.28	147	[6]
0.053	0.803	9.07	1.38	137	[7]

*TS sample; **SC sample[6]

Section S2. Optical parameters of bulk gold for 300-2300 nm

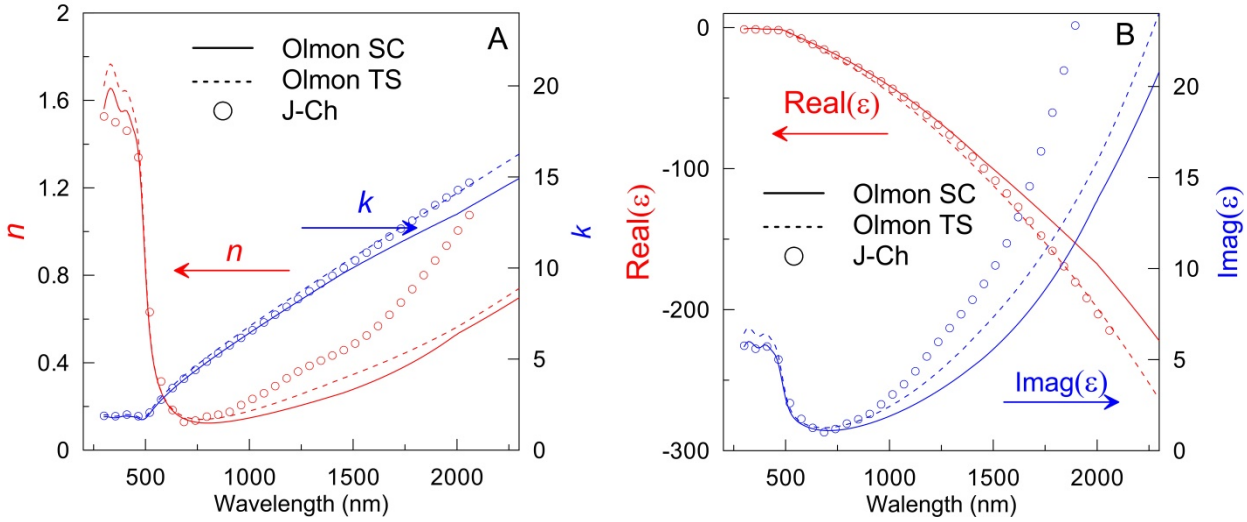

Figure S1. Spectral dependencies of the complex refractive index (A) and the dielectric function (B) by a cubic spline interpolation of tabulated data by Johnson and Christy[2] and Olmon *et al*. (TS and SC samples).[6] Note significant differences between Johnson and Christy and Olmon *et al*. data for wavelengths larger than 1000 nm.

Section S3. Refractive index of water for 300–2300 nm

The refractive index of water has been tabulated in many works (see, e.g., Refs.[8,9] and references therein). The most wide spectral range 182-2770 nm was considered by Thormählen *et al.*[8] who provided the following analytical approximation (in this section, λ is expressed in nm):

$$n = n_{water} = \left[\frac{a_1}{\lambda^2 - \lambda_a^2} + \sum_{i=2}^{5} a_i \lambda^{2i-4} \right]^{1/2}, \qquad \text{(S9)}$$

$\lambda_a^2 = 0.018085$, $a_1 = 5.743534 \times 10^{-3}$, $a_2 = 1.769238$, $a_3 = -2.797222 \times 10^{-2}$, $a_4 = 8.715348 \times 10^{-3}$ $a_5 = -1.413942 \times 10^{-3}$.

In 1998, Harvey *et al.*[10] published a revised dispersion formula which included the dependence of n on the temperature and density. However, for normal conditions at $20^{\circ}\mathrm{C}$, the Eq. (S9) still holds. Bertie and Lan[11] tabulated the real (n) and imaginary (k) parts of water refractive index for the wave numbers between 1500 and 1 cm^{-1}. The authors combined most reliable data for the imaginary part into a single spectrum, from which the real part was calculated by Kramers-Kronig relations. A similar approach was used by Hale and Querry,[12] who tabulated the real and imaginary parts for wavelength range 0.2–200 μm. Daimon and Masumura[13] developed the following analytical Sellmeier equation

$$n = \left[1 + \sum_{i=1}^{4} \frac{a(i)\lambda^2}{\lambda^2 - b(i)} \right]^{1/2}, \qquad \text{(S10)}$$

a(1)=5.684027565E-01, b(1)=5.101829712E-03,

a(2)=1.726177391E-01, b(2)=1.821153936E-02,

a(3)=2.086189578E-02, b(3)=2.620722293E-02

a(4)=1.130748688E-01, b(4)=1.069792721E+01

Similar Sellmeier type approximation was also suggested by Kedenburg *et al.*[14]

$$n = \left[1 + \sum_{i=1}^{2} \frac{A(i)\lambda^2}{\lambda^2 - B(i)} \right]^{1/2}, \qquad \text{(S11)}$$

A(1)=0.75831, B(1)=0.01007, A(2)=0.08495, B(2)=8.91377.

To extend our previous Cauchy type dispersion formula,[15] we introduced an additional correction term (last term in Eq. (S12))

$$n_2 = n_{water} = 1.3233 + \frac{3.478\times10^{-3}}{\lambda^2} - \frac{5.111\times10^{-5}}{\lambda^4} - \frac{\lambda^4}{700},\ [\lambda] = \mu\text{m}. \qquad \text{(S12)}$$

In Figure S2 we compare Eq. (S12) with five tabulated and analytical data sets. In general, Eq. (S12) provides very reliable approximation for wavelengths between 300 and 2200 nm.

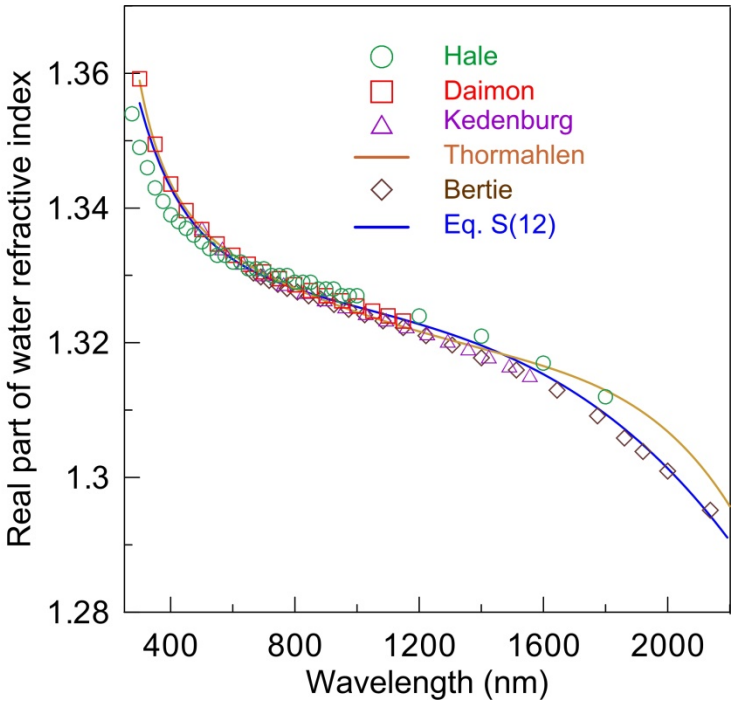

Figure S2. The real part of water refractive index calculated by Eq. (S12) in comparison with available data sets from five literature sources.

The imaginary part of water refractive index was tabulated by Hale and Querry[12], Bertie and Lan[11] and Segelstein.[16] The last work is a continuation of the study by Hale and Querry[12] and provides more accurate data for extended spectral range. Bertie and Lan[11] compared their own data with the data by Hale and Querry[12] and found good agreement. Because of very strong variation of water k values within seven orders of magnitude for wavelengths between 300 and 2300 nm, a direct spline smoothing of k spectrum is not possible. To solve the problem we apply our spline routine to $-\lg(k)$ as function of wavelength (Figure S3A) and then calculated the absorption coefficient

$k = 10^{-[-\lg(k)]}$ (Figure S3B). This approach gave excellent results and reproduces the original data with high accuracy.

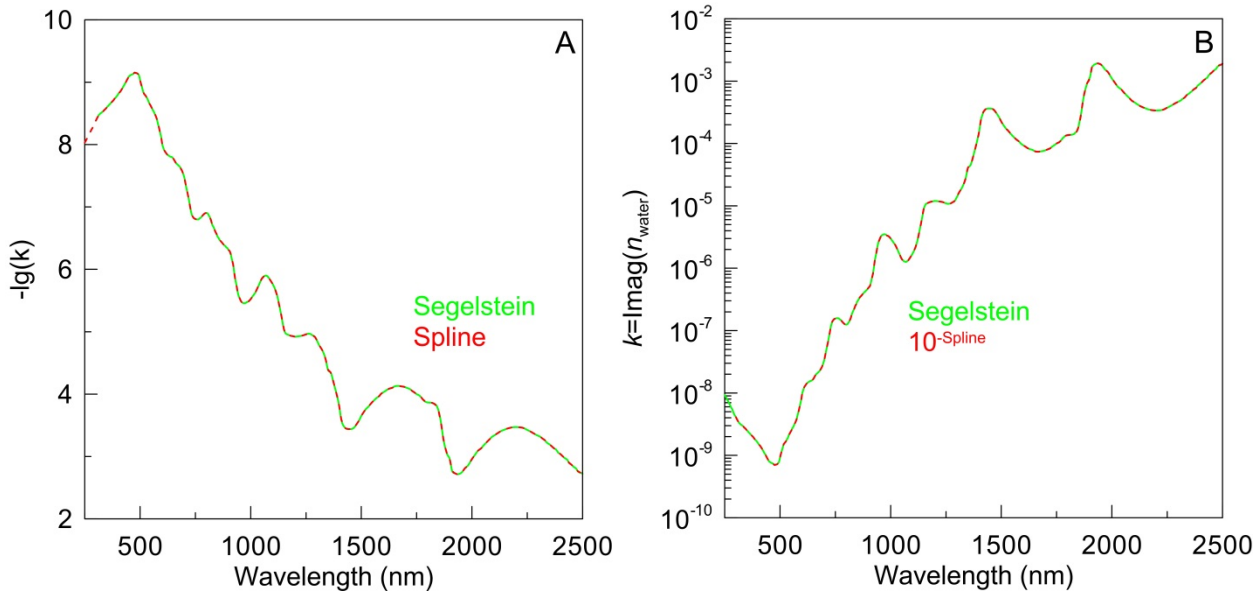

Figure S3. The imaginary part of water refractive index by Segelstein[16] (green line) and a cubic spline approximation (dashed red line). Nice agreement between tabulated and spline data is clearly seen.

Section S4. Small gold spheres and spheroids in an absorbing medium

We calculated the extinction and scattering cross sections for small god spheres and spheroids embedded in a water-like absorbing medium. For small spheres in an absorbing medium, some deviations from dielectric host medium are observed only for wavelengths greater than 1000 nm, where the sphere extinction is very small, from two to three orders of magnitude smaller than the cross section value at resonance.

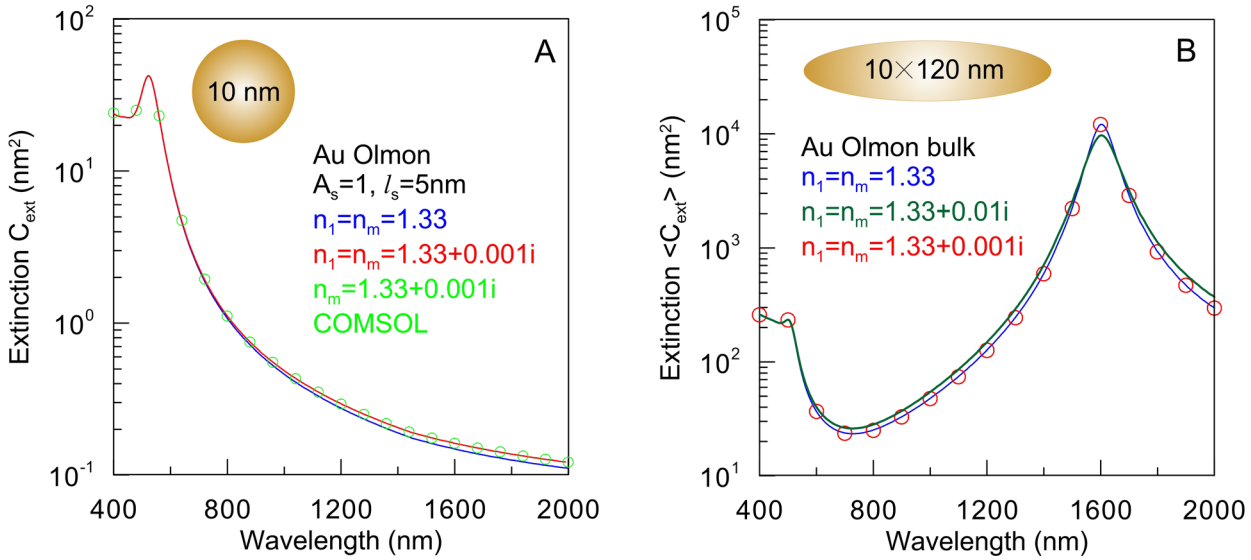

Figure S4. Extinction spectra of 10-nm gold spheres (A) and 10x120-nm randomly oriented spheroids (B) embedded in non-absorbing (1.33+*i*0) and absorbing water-like media with the refractive index $n_1 = 1.33 + 0.01i$ and $n_1 = 1.33 + 0.001i$. Calculations were carried out by Eqs. (8) and (9) of the main text and by COMSOL (green line for spheres). For spheres, the size-corrected dielectric function by Olmon was used with $A_s = 1$ and $l_s = R_{core} = 5$ nm. For spheroids, the bulk Olmon constants were used.

Figure 4 of the main text and Fig. S4 show that the water absorption can be neglected in calculations of the light scattering, absorption (Fig.1) and extinction (Fig. S4) cross sections for all wavelengths between 300 and 2300 nm. Furthermore, COMSOL simulations are in excellent agreement with analytical solution for small spheres. Therefore, in what follows we provide the simulation data obtained for water refractive index as given by Eq. (S12).

Section S5. Geometrical model of a 6-spike AuNA and the scattering geometry used for simulations

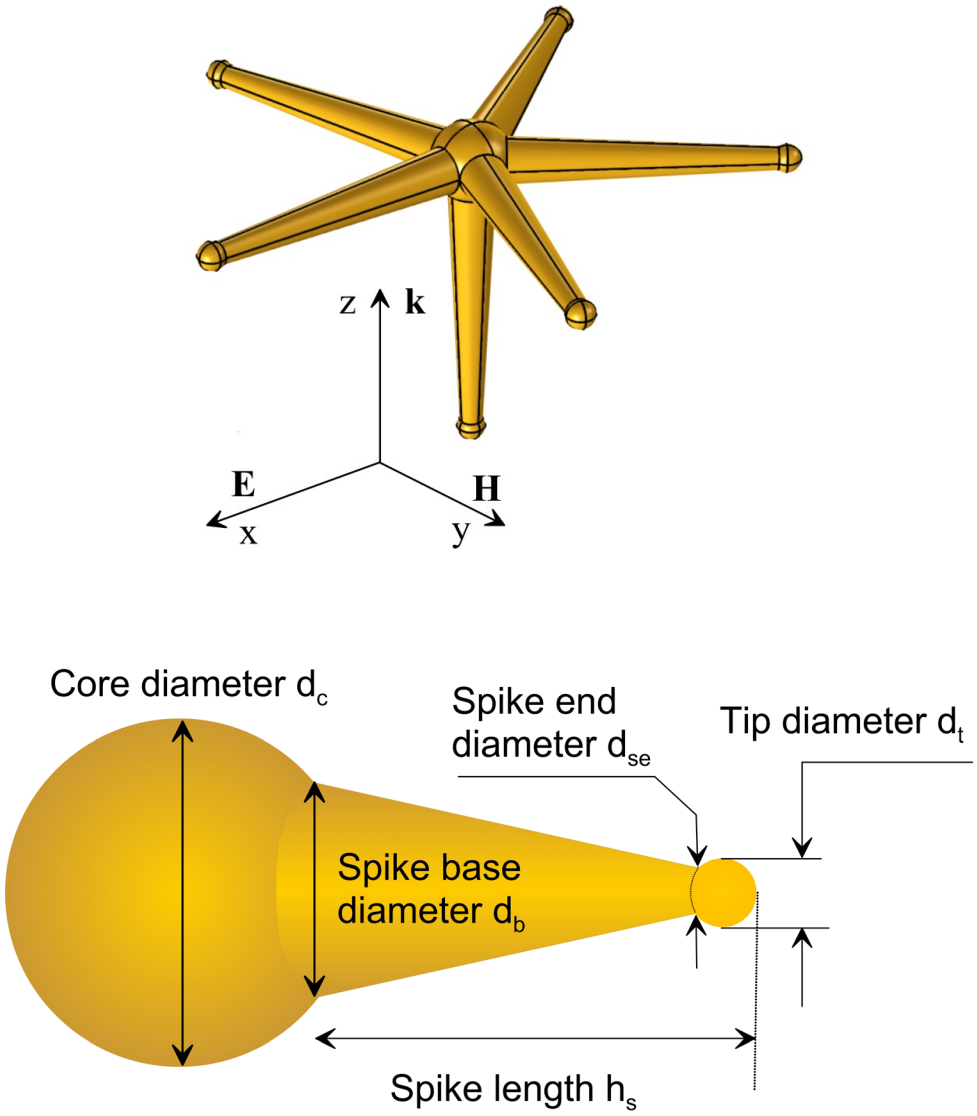

Figure S5. The geometrical model of a 6-spike AuNA and the scattering geometry used for simulations. The incident plane wave propagates along the bottom *z*-spike and is polarized along the side *x*-spike. The bottom picture shows the geometrical definitions: the core diameter $d_c = 23$ nm, the spike length (height) $h_s = 78.5$ nm, the base spike diameter $d_b = 13.2$ nm, the spike end diameter $d_{se} = 6.4$ nm, and the spike tip diameter $d_t = 8$ nm.

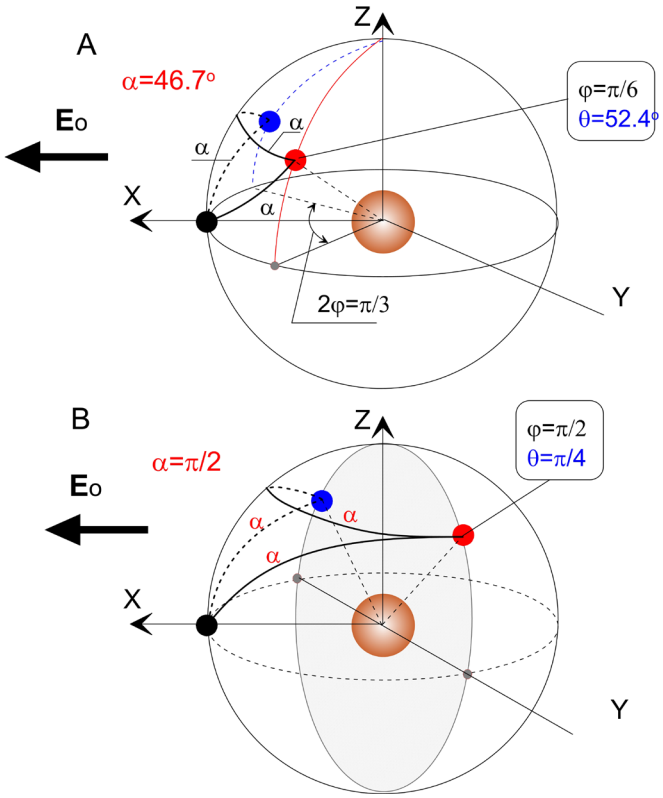

Figure S6. The scattering geometry defining the orientation of three spikes (black, red, and blue) on a sphere. The spike orientation is defined by the angle α of a spherical triangle (the spherical triangle side). The electric field is directed along the *x*-axis and the wave vector is directed along the *z*-axis. For top scheme (A), the angle $\alpha = 46.7^{\circ}$ (see below) and the spherical angles of red and blue spikes are $\theta = 52.4^{\circ}$ and $\varphi = \pm\pi/6$. For bottom scheme (B), the angle $\alpha = \pi/2$ and the spherical angles of red and blue spikes are $\theta = \pi/4$, $\varphi = \pm\pi/2$.

From spherical trigonometry we have $\cos\alpha = \cos^2\theta + \sin^2\theta\cos 2\varphi$ and $\cos\alpha = \sin\theta\cos(\varphi)$.

(1) Let $\varphi = \pi/4$. Then $\cos^2\theta = \frac{1}{\sqrt{2}}\sin\theta$, which gives $\theta = \pi/4$.

Therefore, $\cos\alpha = \frac{1}{2}$ and the spherical triangle side is $\alpha = \pi/3$.

(2) Let $\varphi = \pi/6$. Then the angle θ is determined by equation $\cos^2\theta + \frac{1}{2}\sin^2\theta = \frac{\sqrt{3}}{2}\sin\theta$, or

$x^2 + \sqrt{3}x - 2 = 0$ with $x = \cos\theta$. The solution reads $\theta = \arcsin\frac{\sqrt{11}-\sqrt{3}}{2} = 52.4^{\circ}$.

The spherical triangle side is given by expression $\cos\alpha = \frac{\sqrt{11}-\sqrt{3}}{2}\frac{\sqrt{3}}{2} = \frac{\sqrt{33}-3}{4}$, which gives

$\alpha = 46.7^{\circ}$.

(3) Let $\varphi = \pi/2$. Then $\cos\alpha = \sin\theta\cos(\pi/2) = 0$, $\alpha = \pi/2$, or $3\pi/2$.

$0 = \cos^2\theta - \sin^2\theta = \cos 2\theta$, $\theta = \pi/4$, or $3\pi/4$.

Section S6. Absorption and scattering spectra of AuNST models

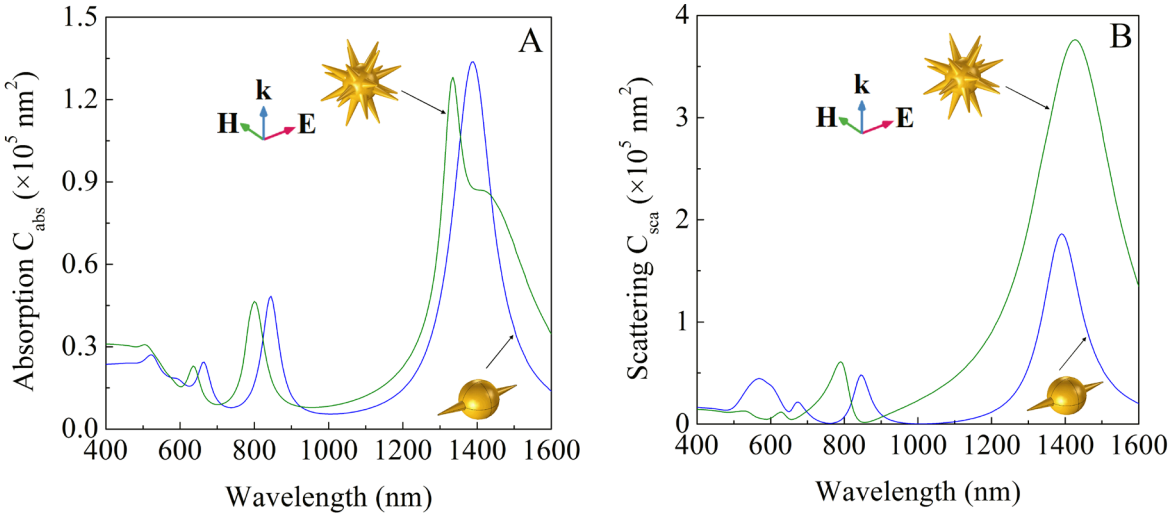

Figure S7. Absorption (A) and scattering (B) spectra of a 20-spike AuNST in water (green curve). The blue absorption and scattering spectra were calculated for a simplified model with only two collinear spikes and illustrate close similarity with spectra for the 20-spike nanostar. In all calculations, the bulk SC constants[6] of Au and non-absorbing water refractive index by Eq. (S12) were used. The core diameter is $d_c = 130$ nm, the spike length $h_s = 90$ nm, the base spike diameter is $d_b = 30$ nm, and the spike tip diameter is $d_t = 4$ nm. Note that the spike end and tip diameters are the same for this model, i.e. $d_{se} = d_t$.

The main result of calculations is that the simple 2-spike model gives reasonable absorption and scattering spectra for a realistic 20-spike model. In any case, the simplified model reproduces all plasmonic peaks and their relative spectral positions.

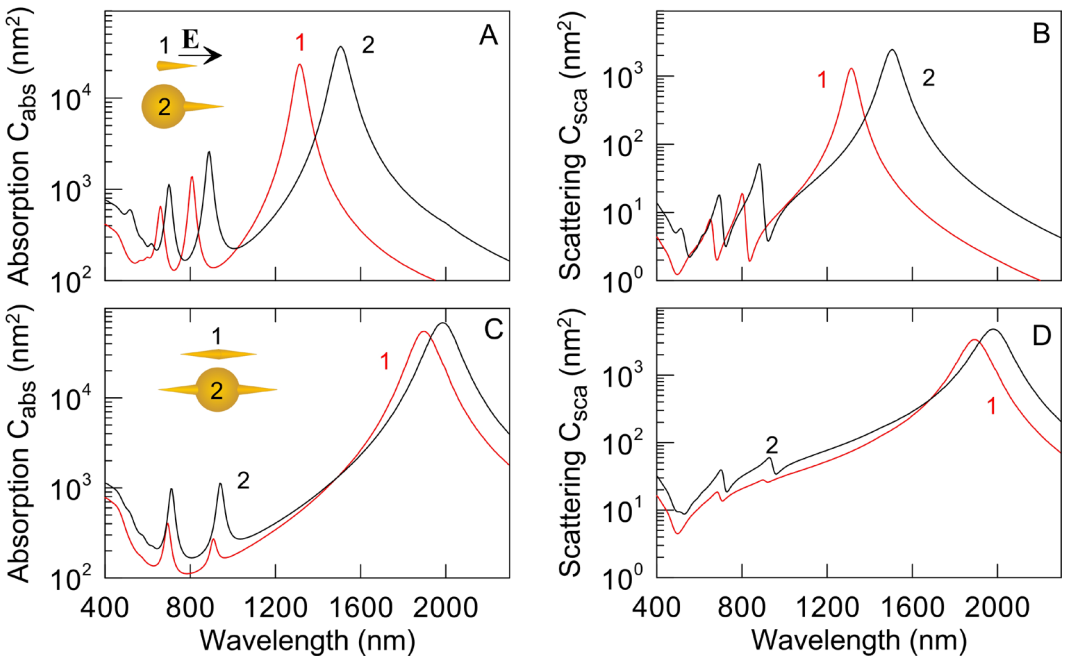

Figure S8. Absorption (A, C) and scattering (B, D)) spectra of cone, cone-on-sphere, bicone, and sphere+2 cones. The arrow shows the field direction. The dipolar plasmon resonances of a single cone and cone-on-sphere are strongly blue-shifted, whereas the higher resonances roughly correspond to those for 2- and 3-spike AuNSTs. All geometrical parameters correspond to those in Fig. S7. The bulk Olmon constants for Au were used for the core and spikes.

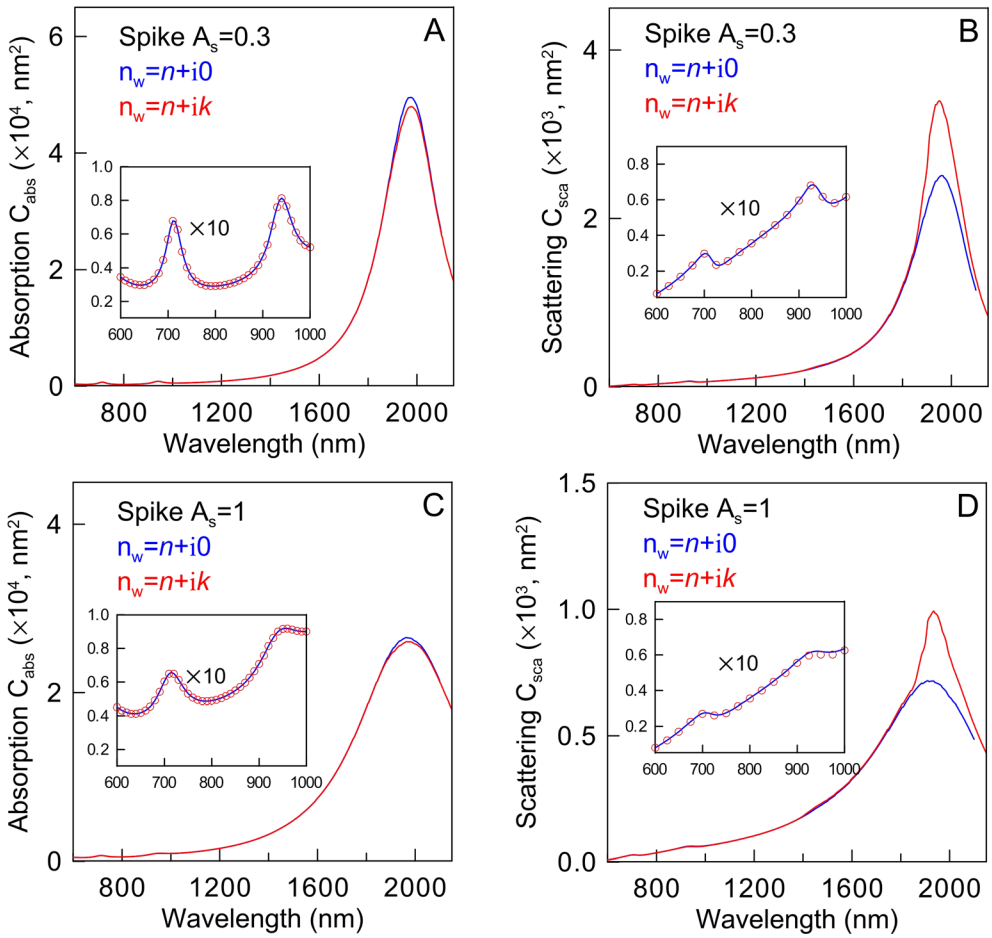

Figure S9. Same as in Fig. 4 but for size corrected dielectric functions with the damping parameter $A_s = 0.3$ (A, B) and 1 (C, D).

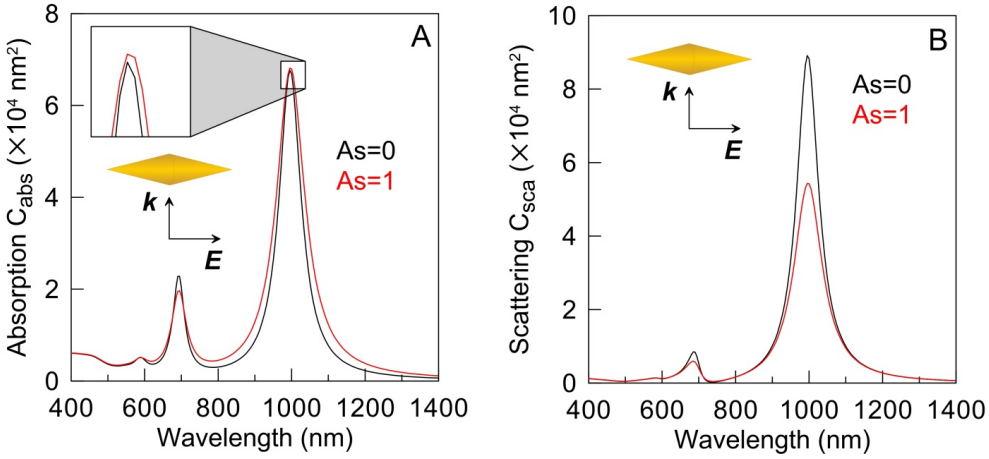

Figure S10. Absorption (A) and scattering (B) spectra of a gold bicone (length, 180 nm, width, 50 nm) at longitudinal excitation. The effective scattering length parameter l_s equals the equivolume radius 29.1 nm, the surface electron scattering parameter A_s equals 0 (black curves) and 1 (red curves). Note that the absorption peak at $A_s = 1$ is untypically greater than at $A_s = 0$, whereas the scattering peak demonstrates a typical decrease for $A_s = 1$.

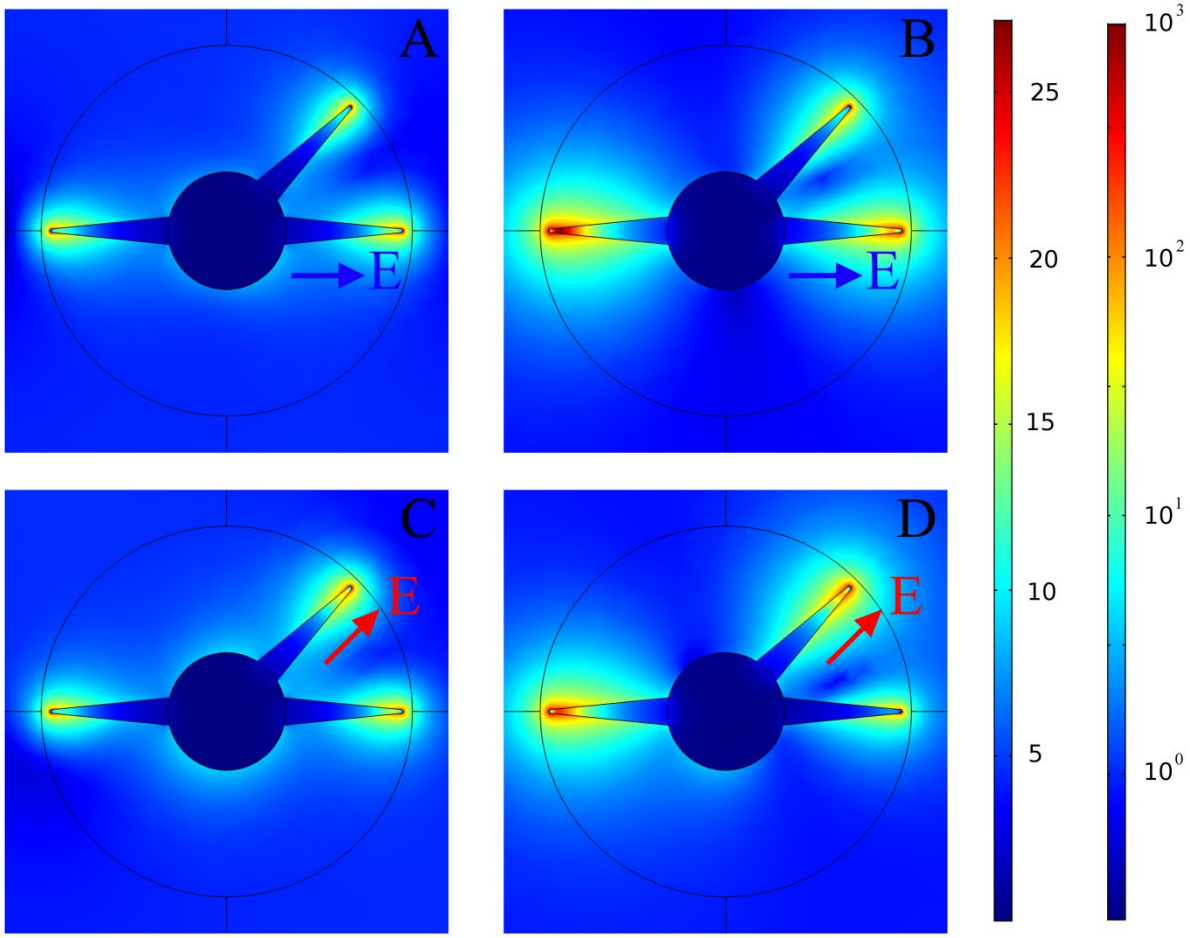

Figure S11. 2D field distribution of $|\mathbf{E}|$ calculated for a 3-spike AuNA at 1550-nm (A, C) and resonance 1870-nm (B, D) excitations along the collinear spike pair (A, B) and along the 45-degree spike (C, D). Note that the excitation wavelength 1550 nm corresponds to the spectral shoulders in Figure 2E, F. The left colour scale is for the field distribution in spike and the right colour scale is for the field distribution in water. Note that at the resonance 1870 nm wavelength, the left collinear spike is excited strongly as compared to the right one (B, D).

Section S7. Dependence of AuNA absorption spectra on polarization: a simple electrostatic model

Consider $N > 2$ identical NA spikes ($S_0, S_1, \cdots S_{N-1}$) located in (x, y) plane (see Fig. S12).

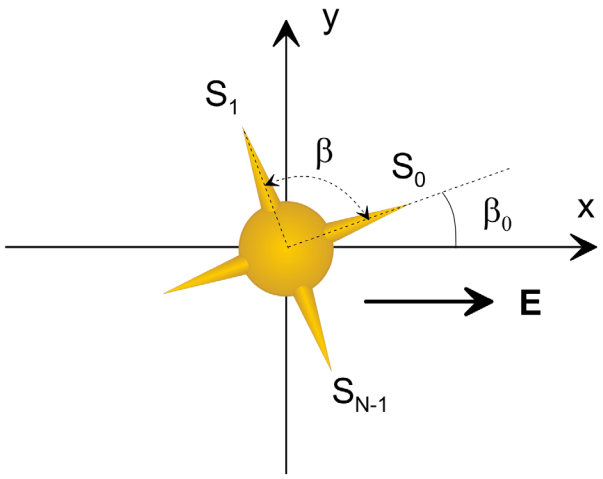

Figure S12. Schematics of an AuNA with 4 spikes located in (*x,y*) plane.

The angle between any neighbouring spikes is constant and equals $\beta = 2\pi / N$. Let the electric field vector **E** be directed along the *x*-axis and the angle between the field and the initial zero spike S_0 equals β_0. Therefore, the angle between the field and an arbitrary spike equals $\beta_n = \beta_0 + n\beta = \beta_0 + 2n\pi / N$, $n = 0,1,\ldots N-1$. In electrostatic approximation, the absorption cross section should be roughly proportional to the squared component of electric field along each spike:

$$C_{abs} = K\sum_{n=0}^{N-1}|E\cos\beta_n|^2 = \frac{K|E|^2}{2}\sum_{n=0}^{N-1}[1+\cos(2\beta_n)] = \frac{K|E|^2}{2}[N+\mathrm{Re}\sum_{n=0}^{N-1}\exp(i2\beta_n)] =$$
$$\frac{K|E|^2}{2}[N+\mathrm{Re}\cdot\exp(i2\beta_0)\sum_{n=0}^{N-1}\{\exp(i2\beta)\}^n] = \qquad (S13)$$
$$\frac{K|E|^2}{2}[N+\mathrm{Re}\cdot\exp(i2\beta_0)\frac{1-\exp(i2\frac{2\pi}{N}N)}{1-\exp(i2\beta)}] = \frac{K|E|^2}{2}[N+0],$$

where the constant K does not depend on the field and the spike orientations. Thus, the absorption cross section does not depend on orientation of the electric field in the (x, y) plane and is proportional to the number of spikes.

For a 6-spike model shown in Fig. S5, five spikes are located in the (*x,y*) plane and one spike is directed along the *z*-axis. Thus, the ratio of cross section for $\mathbf{E}$ located in the (*x,y*) plane to the cross section for *z*-directed field is $\frac{1}{2}5/1=2.5$. When the field $\mathbf{E}$ is oriented at an angle of $\pi/4$ with respect to the *z*-axis, the absorption cross section reads

$$W_{abs}(45)=\frac{K\,|\,E\sin(\pi/4)\,|^2}{2}\cdot 5+K\,|\,E\cos(\pi/4)\,|^2=3.5\,.$$

Finally, for above three orientations of the field we get the following proportion between the peak absorption cross sections $C_{(x,y)}:C_{\pi/4}:C_z=5:3.5:2$, which is in good agreement with numerical simulations shown in Fig. 7 of the main text.

Section S8. Modelling of extinction spectra for colloids and bilayers on glass in air

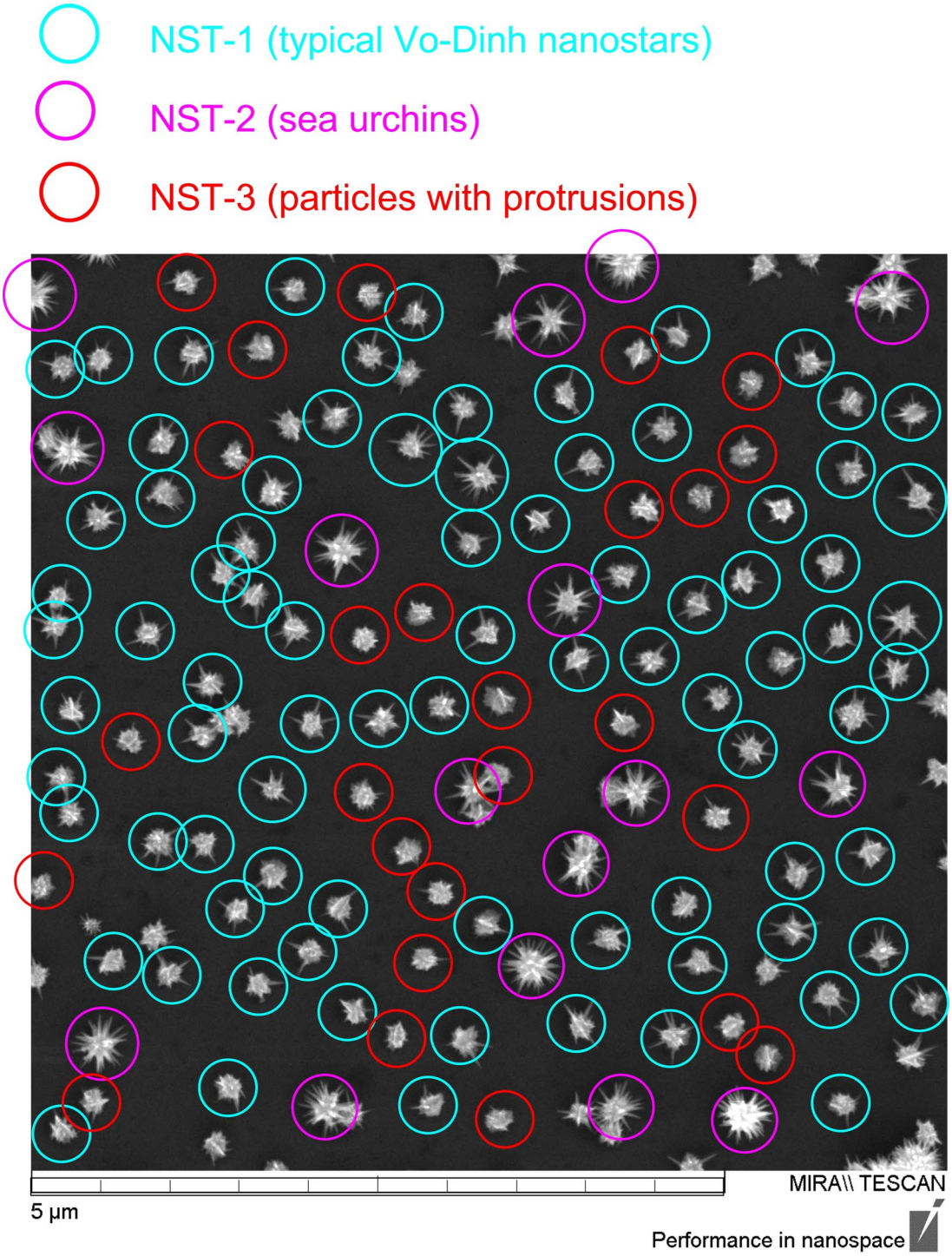

Figure S13 Three types of AuNSTs as revealed from a typical SEM picture.

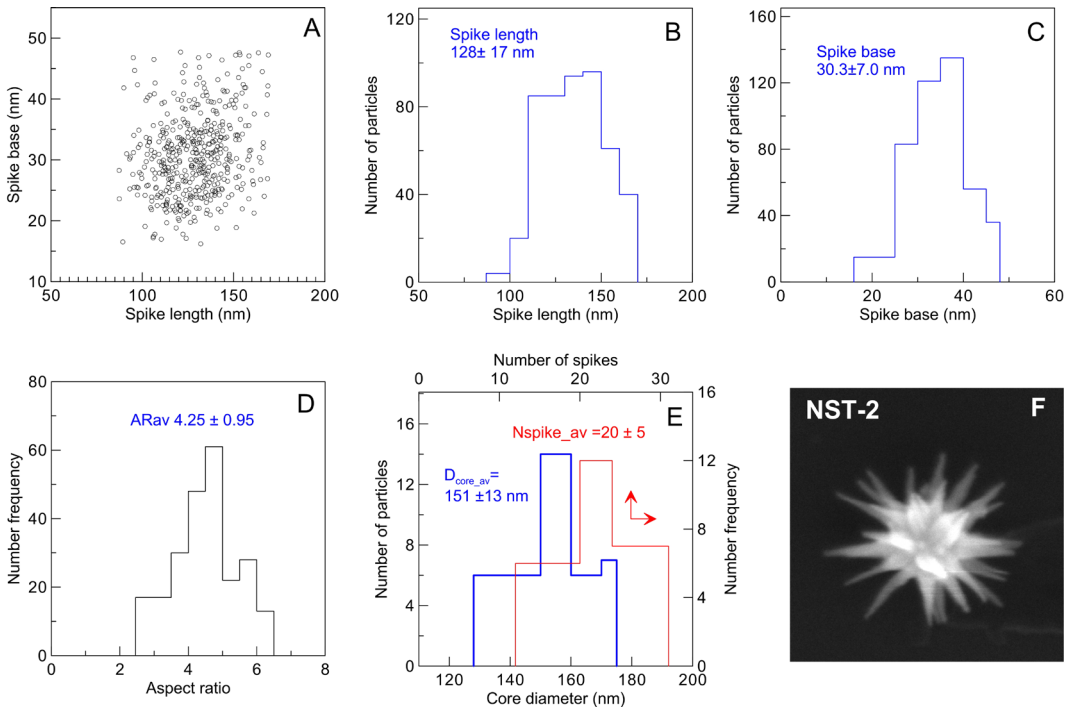

Figure S14. Statistical parameters of NST-2 nanostars derived from SEM images of AuNST-1000-1900 sample (F). In contrast to Fig. 10A of the main text, the spike length-base plot (A) clearly indicates the presence of a single homogeneous ensemble. Next plots show statistical distributions of spike length (B), base (C), and aspect ratio (D). Panels E and F show the core diameter and the number of spikes histograms and a typical morphology of NST-2 nanostars (sea urchins). The average spike number per particle equals 20, the average number percentage of NST-2 particles is 12%. The average geometrical sizes are indicated on the plots.

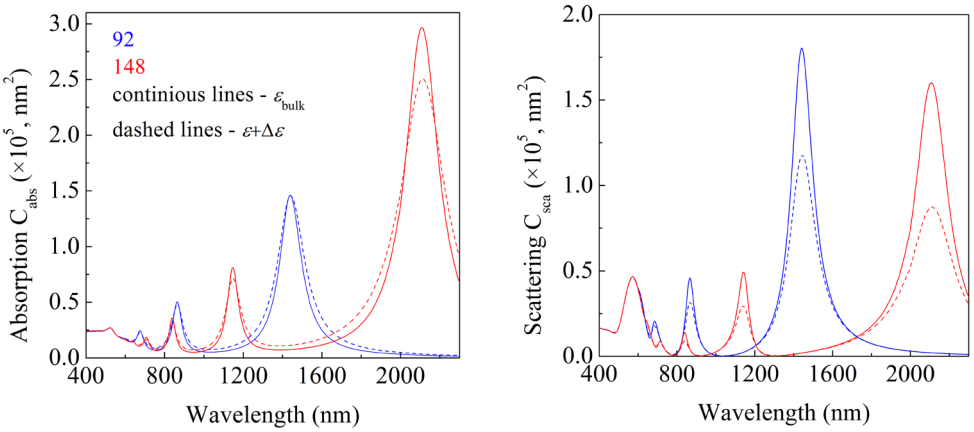

Figure S15. Absorption and scattering spectra of two-spike AuNSTs calculated for bulk (solid lines) and size-corrected (dashed lines) dielectric functions. The spike lengths are 92 (blue) and 148 nm (red). These plots show that the smaller scattering cross sections of AuNSTs with longer spikes cannot be explained by the size-correction effect because for both dielectric functions we observe the same tendency.

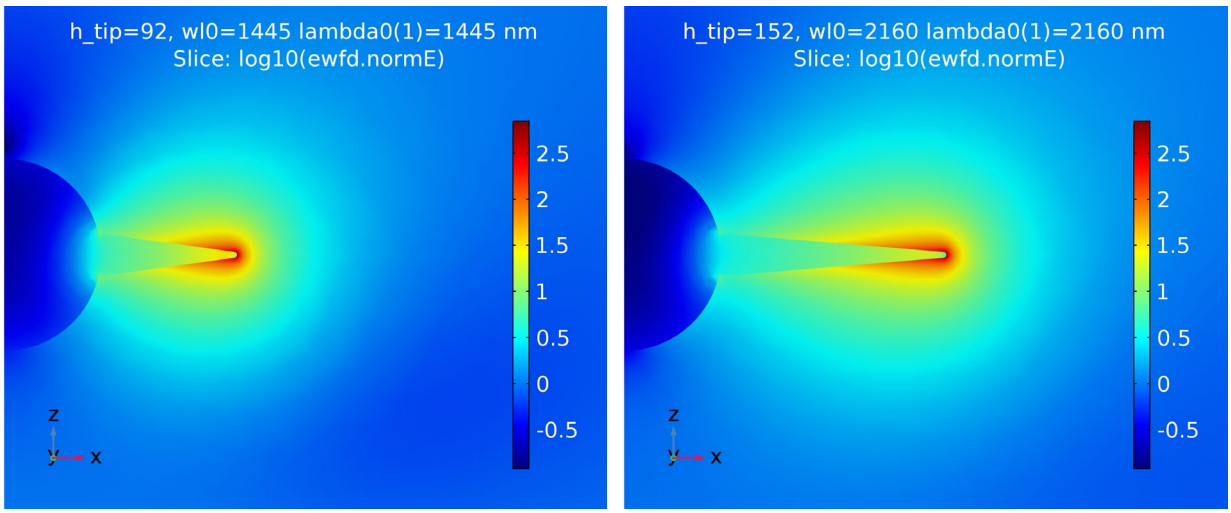

Figure S16. 2D slices of E-field norm calculated for resonance wavelengths of 2-spike AuNAs with short (92 nm, left) and long (152 nm, right) spikes. The core diameter equals 130 nm, the spike base equals 28.8 nm, the incident field is directed along the spike axis. The local field of the short spike is located closer to the core and excites it stronger compared to the long spike field, which is moved to the spike end. This explains why the resonance cross section of a short spike is greater than that for a long spike.

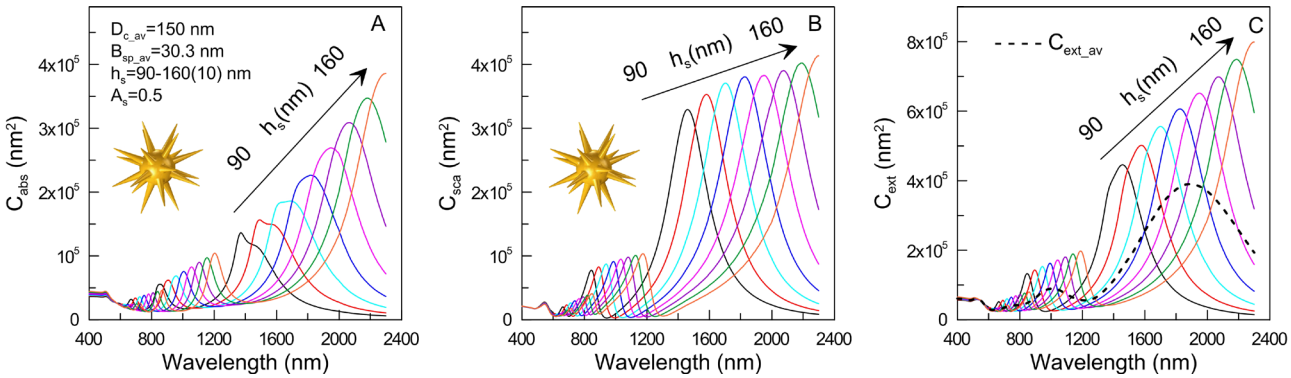

Figure S17. Absorption (A), scattering (B), and extinction (C) spectra of NST-2 AuNSTs in water. The spectra were calculated for the statistical distribution of the spike length, as illustrated by the histograms in Fig. S14. The dashed lines show the histogram-averaged extinction cross sections.

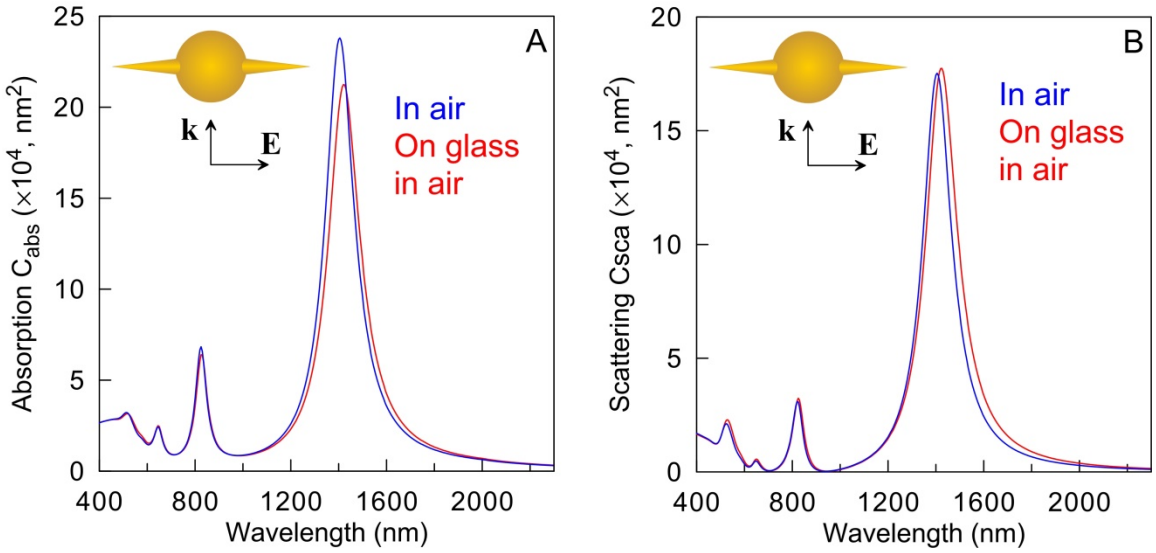

Figure S18. Absorption (A) and scattering (B) spectra of two-spike AuNSTs in air (blue) and on a 0.15 mm glass substrate in air (red). The particle is located on glass/air interface and is illuminated by light travelling from glass to air. The particle parameters are: the core diameter, the spike length and the spike base radius are 130, 130 and 15 nm, respectively. The effective path length is $l_s = 20$ nm and the dumping parameter is $A_s = 0.5$.

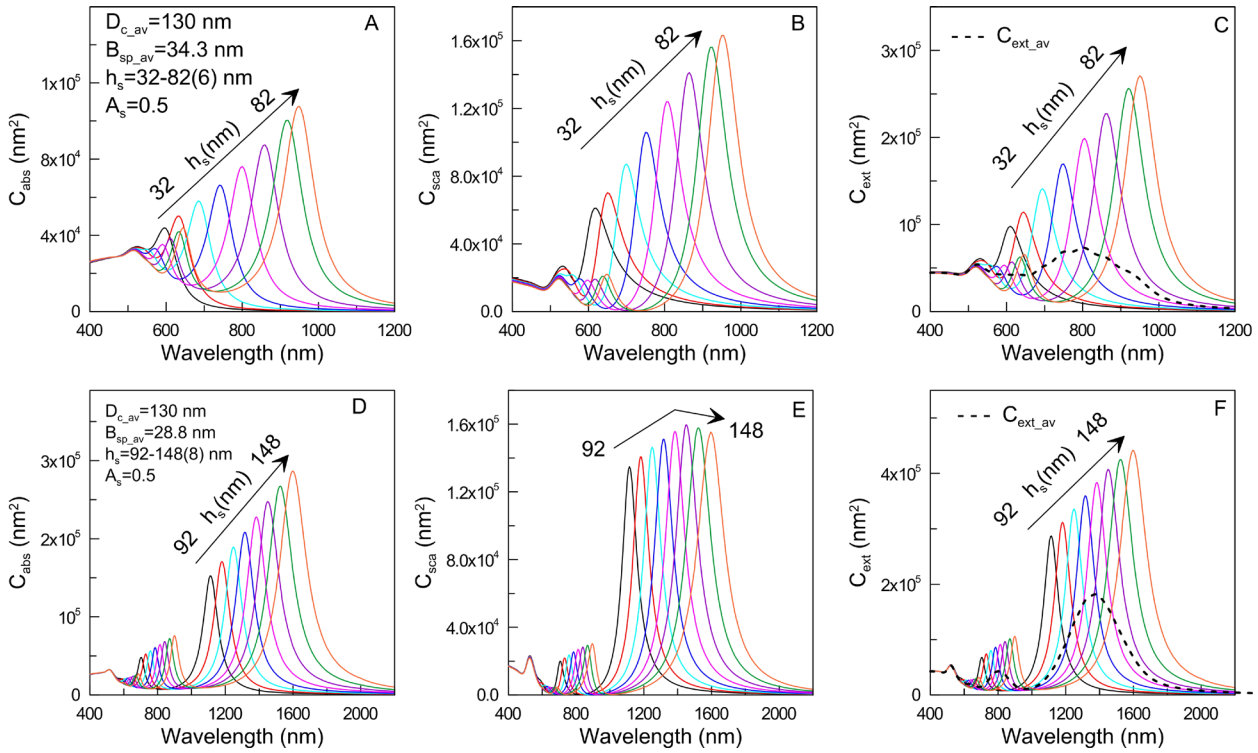

Figure S19. Absorption (A,D), scattering (B,E) and extinction (C,F) spectra of two-spike AuNSTs in air calculated for NST-1A and NST-1B statistical subensembles of spikes as illustrated by histograms in Fig. 10 of the main text. The dashed lines show the histogram-averaged extinction cross sections of two subensembles. In general, these plots are similar to those shown in Fig. 12 for nanostars in water, except for expected shift to the blue (200 nm for NST-1A and 400 nm for NST-1B). Note a small decrease in the resonance scattering cross section with an increase in the spike length for three last spectra (panel E).

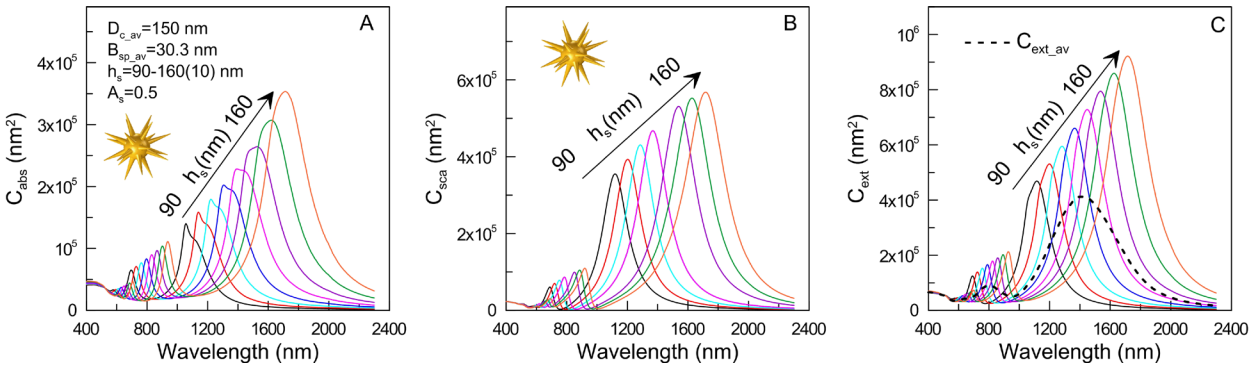

Figure S20. Absorption (A), scattering (B) and extinction (C) spectra of NST-2 AuNSTs in air calculated for statistical distribution of spike length as illustrated by histograms in Fig. S14. The dashed lines show the histogram-averaged extinction cross section.

Section S9. Additional SEM and TEM images of AuNST-1000-1900 particles.

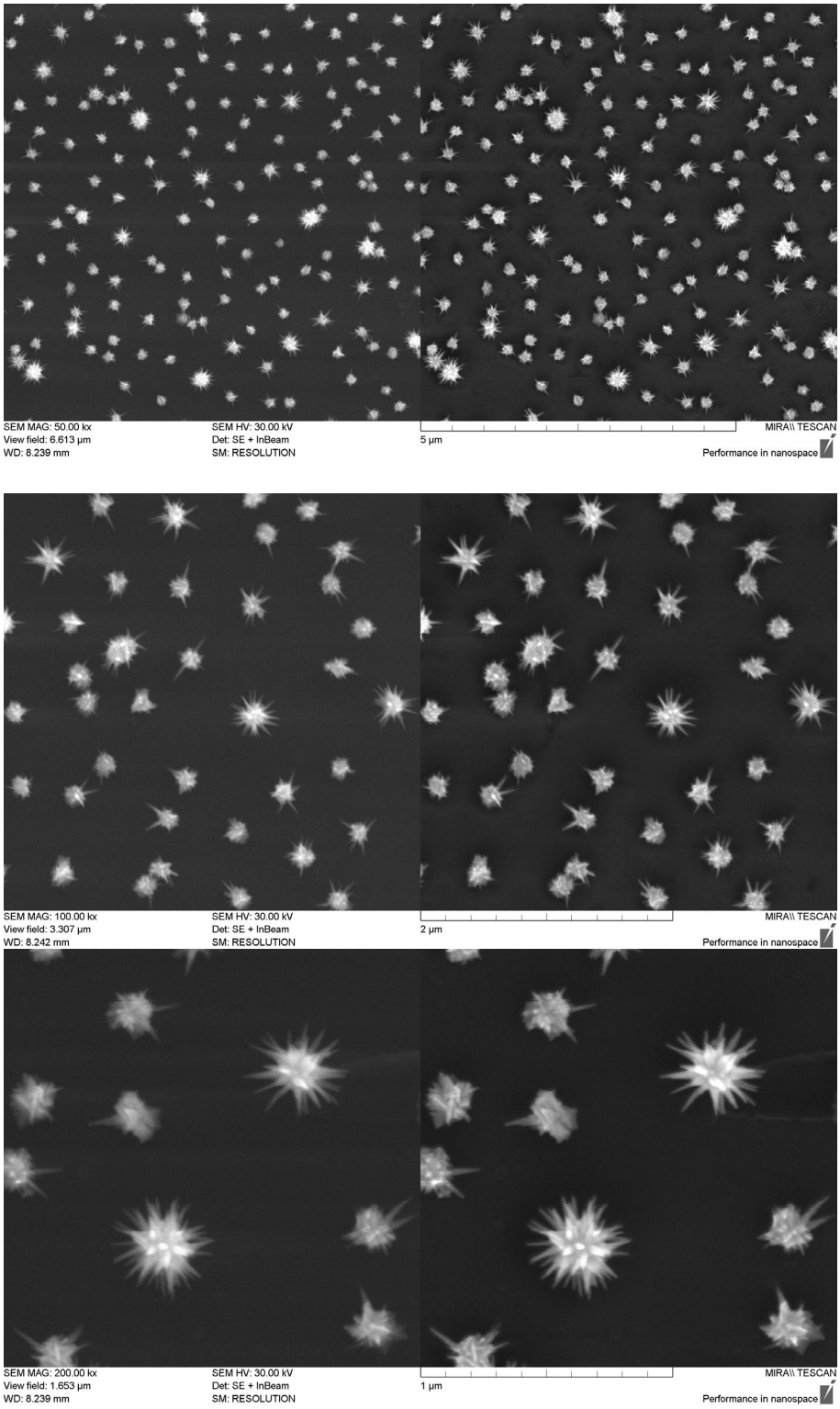

Figure S21. SEM images of AuNST-1000-1900 particles at different magnifications. The scale bars are 5, 2, and 1 µm

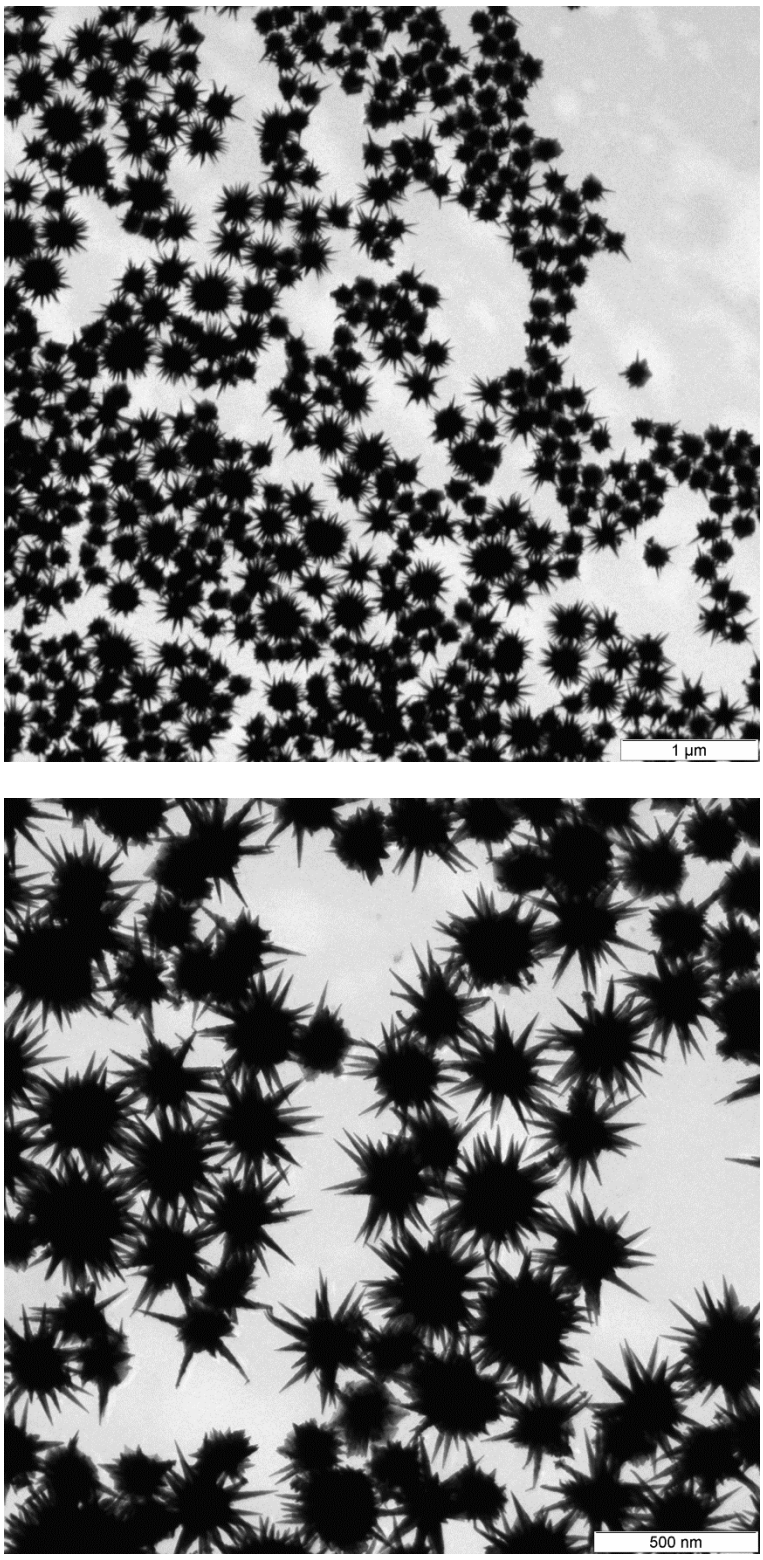

Figure S22. TEM images of AuNST-1000-1900 particles at two magnifications. The scale bars are 1000 and 500 nm.

References

1. Granqvist, C. G.; Hunderi, O. Optical Properties of Ultrafine Gold Particles, *Phys Rev B* **1997**, *16*, 3513.
2. Johnson, P. B.; Christy, R. W. Optical Constants of the Noble Metals. *Phys. Rev. B* **1972**, *6*, 4370–4379.
3. Underwood, S.; Mulvaney P.; Effect of the Solution Refractive Index on the Color of Gold Colloids. *Langmuir* **1994**, *10*, 3427–3430.
4. Oubre, C.; Nordlander P. Optical Properties of Metallodielectric Nanostructures Calculated Using the Finite Difference Time Domain Method. *J. Phys. Chem. B* **2004**, *108*, 17740–17747.
5. Mendoza Herrera, L. J.; Arboleda, D. M.; Schinca, D. C.; Scaffardi, L. B. Determination of Plasma Frequency, Damping Constant, and Size Distribution from the Complex Dielectric Function of Noble Metal Nanoparticles. *Appl. Phys*. **2014**, *116*, 233105.
6. Olmon, R. L.; Slovick, B.; Johnson, T. W.; Shelton, D.; Oh, S.-H.; Boreman, G. D.; Raschke, M. B. Optical Dielectric Function of Gold. *Phys. Rev. B* **2012**, *86*, 235147.
7. Rakić, A. D.; Djurišić, A. B.; Elazar, J. M.; Majewski, M. L. Optical Properties of Metallic Films for Vertical-Cavity Optoelectronic Devices. *Appl. Opt*. **1998**, *37*, 5271–5283.
8. Thormählen, I.; Straub, J.; Grigull, U. Refractive Index of Water and its Dependence on Wavelength, Temperature, and Density. *J. Phys. Chem. Ref. Data* **1985**, *14*, 933–945.
9. Rakić, A. D. URL: https://refractiveindex.info/ Last link 20.02.2020.
10. Harvey, A. H., Gallagher, J. S.; Sengers, J. M. H. L. Revised Formulation for the Refractive Index of Water and Steam as a Function of Wavelength, Temperature and Density. *J. Phys. Chem. Ref. Data* **1998**, *27*, 761–774.
11. Bertie, J. E.; Lan, Z. Infrared Intensities of Liquids XX: The Intensity of the OH Stretching Band of Liquid Water Revisited, and the Best Current Values of the Optical Constants of H_2O at 25°C between 15,000 and 1 cm^{-1}. *Appl. Spectrosc*. **1996**, *50*, 1047–1057.
12. Hale, G. M.; Querry, M. R. Optical Constants of Water in the 200-nm to 200-Mm Wavelength Region. *Appl. Opt*. **1973**, *12*, 555–562.
13. Daimon, M.; Masumura A. Measurement of the Refractive Index of Distilled Water From the Near-Infrared Region to the Ultraviolet Region. *Appl. Opt*. **2007**, *46*, 3811–3820.
14. Kedenburg, S.; Vieweg, M.; Gissibl, T.; Giessen, H. Linear Refractive Index and Absorption Measurements of Nonlinear Optical Liquids in the Visible and Near-Infrared Spectral Region. *Opt. Mater. Express* **2012**, *2*, 1588–1611.
15. Khlebtsov, N. G.; Bogatyrev, V. A.; Dykman, L. A.; Melnikov, A. G. Spectral extinction of colloidal gold and its biospecific conjugates. *J. Colloid Interface Sci*. **1996**, *180*, 436–445.

16. Segelstein, D. J. The complex refractive index of water. Master Thesis (1981). Note: This is a continuation of work by Hale and Querry (1973) providing improved data and extended range.